International Journal of Scientific Research in Engineering and Management (IJSREM)
Volume: 10 Issue: 01 | Jan - 2026 SJIF Rating: 8.586 ISSN: 2582-3930

Amplifying Absorptive Elimination of Alizarin Red S Dye from Contaminated Water Through Chemically Improved *Arachis Hypogeal* By-Product and Optimizing Thermodynamics, Kinetics and Adsorption Isotherm

Anjna Kumari, Anita Rani and Ajay Sharma
Department of Chemistry, IEC School of Basic and Applied Sciences, IEC University, Baddi, Solan, (H.P.) India 174103

Abstract:
This study introduced two effective and affordable organic and metal based hydrochars named ASB and ASB/LaCF, in the reservoir of eco-friendly and environmental friendly substances. The shell of ***Arachis hypogeal*** was utilized to synthesize organic biochar (ASB) while combination of three metal salts *viz.* Lanthanum nitrate ($La(NO_3).6H_2O$), ferric nitrate ($Fe(NO_3).6H_2O$) and cobalt nitrate ($CoNo_3).6H_2O$ i.e. (LaCF) was incorporated in the bulk of biochar (ASB) to obtain nanocomposite (ASB/LaCF). FTIR study reveal the nature of functional groups available in the organic moiety after formation of biochar as well as nanocomposite. SEM and XRD reveal the amorphous nature of ASB and slight crystalline behaviour of ASB/LaCF. VSM analysis describe the magnetic property and magnetization value for ASB/LaCF was observed as 0.354 emu/g. BET analysis identified pore size of 3.2 nm and 7.5 nm for ASB and ASB/LaCF respectively while surface area for ASB/LaCF was 52.25 m^2/g. TGA and DSC graphs throw light on thermal stability of the nanocomposite where 50% weight loss was observed till 200ºC and upto 700 ºC, no change in graph was observed. Similar pattern was identified in DSC curve. Thermodynamic and kinetic parameters were analysed through adsorption of Alizarin red S dye as a pollutant and the results were amazing as the synthesized ASB and ASB/LaCF were able to remove the dissolved dye from the water sample by changing different reaction conditions like Temperature, concentration, pH and time etc.
Keywords: Biochar; Nanocomposite; Adsorption; Thermal study; Kinetic study, pollutant removal

Corresponding author: Dr. Anita Rani
Email id: caoudhary.anita@gmail.com
ORCID id: 0000-0002-3599-7563

Introduction:

Biochar drawn from plant waste has materialized as a sustainable and flexible material with substantial environmental and industrial applications. Produced through the pyrolysis of agricultural residues, forestry waste, and other plant-based biomass, biochar is a carbon-rich, porous solid known for its high surface area, stability, and functional surface groups **[1-3]**. Utilizing plant waste for biochar production not only provides an effective method for recycling organic matter but also helps reduce environmental burdens associated with biomass disposal **[4-6]**. The resulting biochar serves as an efficient adsorbent, soil amendment, and support material for catalysts and nanocomposites due to its excellent physicochemical properties. Its ability to immobilize contaminants, enhance soil fertility, and sequester carbon makes plant waste–derived biochar a promising eco-friendly material for applications in water purification, environmental remediation, agriculture, and sustainable waste management **[7-9]**.

Similarly Lanthanum–cobalt ferrite nanocomposites are advanced functional materials known for their remarkable magnetic, electrical, and catalytic properties. Belonging to the class of spinel ferrites, these nanocomposites combine lanthanum, cobalt, and iron oxides in a highly ordered structure that enhances their stability, magnetic responsiveness, and surface reactivity **[10-11]**. Their nanoscale dimensions further improve characteristics such as high surface area, efficient charge transfer, and enhanced adsorption capabilities. Because of these unique features, lanthanum–cobalt ferrite nanocomposites have gained significant attention in fields such as environmental remediation, photocatalysis, sensors, energy storage, and biomedical applications **[12-13]**. Their strong magnetic properties also allow easy recovery from aqueous environments, making them particularly useful for pollutant removal. Overall, lanthanum–

cobalt ferrite nanocomposites represent a promising class of multifunctional materials suitable for various technological and environmental applications.

Combining plant-based biochar with lanthanum–cobalt ferrite nanocomposites creates a highly efficient hybrid material that leverages the strengths of both components for advanced environmental and technological applications. Plant-derived biochar offers a porous structure, large surface area, and abundant functional groups, which enhance the dispersion and stability of ferrite nanoparticles while minimizing their aggregation **[14]**. When integrated with lanthanum–cobalt ferrites, the composite exhibits improved magnetic recovery enhanced catalytic and adsorptive performance, and greater structural integrity. This synergy allows for faster pollutant removal, superior degradation of organic and inorganic contaminants, and increased reusability due to the magnetic separability of ferrites **[15-16]**. Additionally, using plant waste to produce biochar ensures sustainability, cost-effectiveness, and reduced environmental impact. Overall, the combination of plant-based biochar and lanthanum–cobalt ferrite nanocomposites results in a multifunctional, eco-friendly material with exceptional potential in water purification, catalysis, and environmental remediation.

This research article incorporates the fabrication of biochar encapsulated Lanthanum-Cobalt ferrites Nanocomposite (ASB/LaCF), where the biochar (ASB) has been secured from the shell of ***Arachis hypogea*** and the metal nanocomposite attained through the combination of Lanthanum nitrate ($La(NO_3).6H_2O$), ferric nitrate ($Fe(NO_3).6H_2O$) and cobalt nitrate ($CoNo_3).6H_2O$ i.e. (LaCF). Identification of all three components i.e. Biochar (ASB), metal composite (LaCF) and biochar based metal nanocomposite (ASB/LaCF) has been executed by various analytical techniques. Moreover, water purification has been concluded by taking Alizarin red S dye as pollutant and amount of adsorption has been verified by analyzing different thermodynamic and kinetic parameters.

Material and Method:

In this research article, chemicals of the analytical grades were utilized. Alizarin Red S dye with molecular weight 360.28 g/mol, with molecular formula of ($C_{14}H_7NaO_7S$), was attained from Sigma - Aldrich, India with a standard grade. The chosen dye was used for the experiments without any further amendments. Chemicals, namely HCl, H_2SO_4 and NaOH were attained from Merck Life Sciences Private Limited. 1000 milliliters of deionized water was diluted with one gram of Alizarin Red S dye to obtained 1000 mg L^{-1} of stock solution.

Prepration of bio-sorbent from *Arachis hypogea* shell:

The shell of ***Arachis hypogeal*** were collected from Bilaspur (H.P.), India, and thoroughly washed with double-distilled water to remove any adhering impurities. They were then air-dried in sunlight for several days. After drying, the material was chopped, crushed, and ground to obtain a uniform particle size. The resulting powdered sample was stored in a desicator for further analysis.

Preparation of biochar (ASB):

The material was pyrolysed in a furnace at 700 °C for two and a half hours, with the temperature increased by 50 °C every 20 minutes. After pyrolysis, it was allowed to cool overnight. Chemical activation was carried out by immersing the biochar in 5% sodium hydroxide (NaOH) and 6% sodium hypochlorite (NaClO) solutions. The mixture was then exposed to microwave heating at 50–60 °C for 30 minutes. The activated biochar was subsequently filtered and rinsed repeatedly with double-distilled water until the pH reached neutrality (pH 7). Finally, the treated biochar (ASB) was oven-dried at 60 °C overnight and stored for further use.

Synthesis of lanthanum ferrite ($LaFe_2O_3$):

The Lanthanum ferrites were prepared through sol-gel method. For the preparation of Lanthanum ferrites ($LaFe_2O_{3,}$) 0.06M of Lanthanum nitrate ($La(NO_3).6H_2O$) and 0.06M of ferric nitrate ($Fe(NO_3).6H_2O$) were taken and added to 30ml of distilled water. Now 2-3 drops of citric acid ($C_6H_70_8$) were also added to the above solution for maintaining the pH of the solution. The solution was heated by using magnetic stirrer at 80°C for 90 minutes continuously. After heating the yellowish brown gel was obtained which was dried in an oven for 2 hours and then kept at room temperature.

Preparation of Cobalt ferrites ($CoFe_2O_3$):

The cobalt ferrite was prepared through the co-precipitation method. In this method two or more soluble compounds were precipitated from a solution for obtaining the solid. The cobalt ferrite was prepared by taking cobalt nitrate

($CoNo_3$).$6H_2O$ (0.2M) and ferric nitrate $FeNO_3.9H_2O$ (0.6M) and dispersing these two compounds in 30ml of distilled water with continuous stirring of the solution for 45 minutes at 50-60℃ temperature. Now 0.2M of NaOH i.e. sodium hydroxide was added dropwise to the solution to form the metal oxides. After adding sodium hydroxide again the solution was stirred upto 1 hour at 80℃.

Synthesis of Lanthanum-Cobalt ferrites (LaCF):

For the preparation of lanthanum cobalt ferrites (LaCF), lanthanum ferrite ($LaFe_2O_3$) was dispersed in 45ml of distilled water in the ratio of 2:1. Now cobalt ferrite ($CoFe_2O_3$) was also added to the above solution with constant stirring and heating at 80℃ temperature for 90 minutes. Brownish precipitates were formed. After that precipitates were washed with distilled water and dry the precipitates in an oven for 1 hour and placed at room temperature.

Synthesis of biochar encapsulated Lanthanum-Cobalt ferrites Nanocomposite (ASB/LaCF):

Nanocomposites of lanthanum–cobalt ferrites (LaCF) with biochar (ASB) were synthesized by adding 3–4 g of activated biochar to 50 mL of distilled water, followed by gradual dispersion and stirring on a magnetic stirrer at room temperature for 90 minutes. The prepared lanthanum–cobalt ferrite precipitates were then introduced into the above mixture. The resulting solution was refluxed in 50 mL water for 4 hours at a temperature of 80–90 °C. After completion, the mixture was allowed to cool, and the precipitates (ASB/LaCF) were filtered and dried in an oven for one hour.

Characterization Techniques:

The optical properties of the synthesized nanocomposite (ASB/LaCF) were first analyzed using a FTIR (PerkinElmer® Spectrum™ 400 FT-IR/NIR spectrometer) to identify different functional groups present in biochar (ASB), metal composite (LaCF) and biochar based metal nanocomposite (ASB/LaCF) so that comparison can be done between them**.** Crystallinity and porosity were evaluated through X-ray diffraction (XRD) analysis (X'Pert Pro XRD models). Surface morphology and particle boundaries were examined using scanning electron microscopy (SEM, Hitachi SU 8010 Series). Additionally, BET (Quantachrome Autosorb-iQ-MP/XR) was deployed to quantify the specific surface area and poresize distribution within the nanoparticles, DSC (Thermo Scientific <<<b/>ArctiX<<!b/> DSC) provided information about thermal stability, homogeneity and dispersion of the synthesized nanoparticles, TGA (RT-2400°C), allows the study of kinetics of chemical reactions, like evaporation, decomposition and stability, by analyzing mass changes over time or temperature. The Barett-Joyner-Halenda (BJH) method was deployed to formulate pore-size distribution curve.

Batch adsorption analysis:

Batch adsorption analysis was deployed in the adsorption process to optimize various parameters. The wetness content in the ASB and ASB/LaCF were expelled by arranging them for 2 hr. in hot air oven at 120º C. The required amount of ASB and ASB/LaCF adsorbents were mixed in an orbital shaker, with the Alizarin red S dye concentration varying from 50 mg/L to 250 mg/L at 303k. After filtering the surplus solution with the Whatman filter paper, the remaining dye was measured by taking help of UV spectrophotometer. The adsorption procedure was repeated up to three times to make sure about the consonant results. The experiment's efficiency (η) and equilibrium adsorption capacity (q_e) and were determined using the following formulas:

$$\eta = (C_0\text{-}C_e \text{ x}100)/C_0 \quad \text{..... (1)}$$

$$q_e = (C_0\text{-}C_e \text{ xV})/m \quad \text{..... (2)}$$

Where C_0 and C_e stand for the initial and final concentrations of the Alizarin red S dye (mg/L), while, q_e denotes the equilibrium adsorption capacity (mg/g^{-1}).

FTIR spectral analysis:

The FTIR study was recorded in the range on 4000-400 cm^{-1} **(Fig 1)**. The spectra of ASB **(Fig 1 (a))** shows the absorption band between 1415 cm^{-1} and 1340 cm^{-1} due to C-C polyphenolic stretching of lignin and plane deformation vibration of aromatic and aliphatic C-H moiety, might be in $-CH_3$, $-CH_2$, $-O-CH_3$ groups. The peaks appeared at 1639 cm^{-1} and 2849 cm^{-1} were ascribed to the carbonyl compounds and amines present in organic moiety **[17]**. FTIR spectrum of LaCF **(Fig 1 (b))** shows a broad peak at 3379 cm^{-1} and minor peak at 2924 cm^{-1} may be due to oxide

stretching and bending vibrations of metals, respectively. While, peak appeared at 718 cm^{-1} is due to La-O bending vibration, at 657 cm^{-1} and 539 cm^{-1} may be due to bending vibrations of Cobalt and iron oxides **[18].**

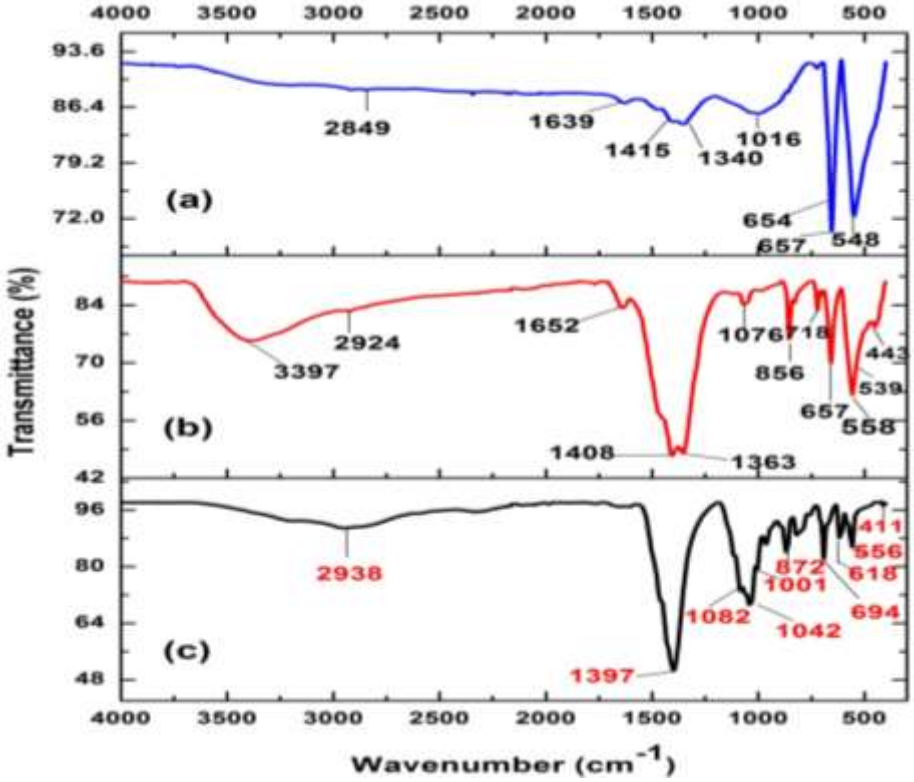

Fig 1: FTIR Spectra of (a) ASB, (b) LaCF and (c) ASB/LaCF

The shifting of metal oxide peaks in ASB/LaCF **(Fig 1 (c))** at 694, 618 and 556 confirmed that lanthanum cobalt ferrite nanoparticles were successfully bonded to the organic moiety of ASB **[19-20]**. Similarly shifting of various peaks in ASB/LaCF compared to ASB and LaCF defines the structural and chemical changes in organic moiety.

XRD analysis:

The XRD spectra of ASB**,** LaFC and ASB/LaCF has been shown in **(Fig 2)**. Very few diffraction peaks at 2θ = 31.22º and 31.96º confirm amorphous nature of the organic biochar ASB **(Fig 2 (a))**. On the other hand **(Fig 2 (b))** defines that the crystalline behaviour of LaCF is highly crystalline with major diffraction peaks at 2θ = 29.52º, 31.38º, 33.40º, 36.02º, 43.71º, 48.69º and 54.20º etc. While the and **(Fig 2 (c))** suggested that the crystallinity declines after incorporation of metals into the core of organic moiety to form ASB/LaCF which reveal major peaks at 20.40º, 23.86º, 30.13º, 36.82º, 44.50º and 65.28º etc. that indicate modification in the structure of biochar ASB and inorganic moiety LaCF, to form ASB/LaCF suggesting the formation of nanocomposite **[21-22]**.

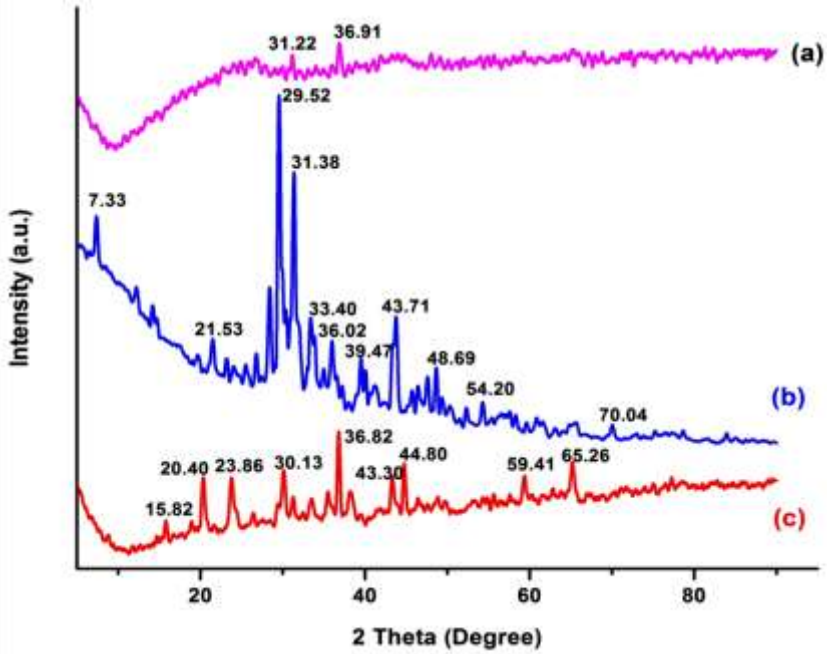

Fig 2: XRD spectra of (a) ASB, (b) LaCF and (c) ASB/LaCF

The average crystalline size was calculated by using Sherrer equation:

$$D = k\lambda/\beta \cos\theta \quad \text{..... (3)}$$

where D = Average crystalline size, λ = wavelength, β = WHM of diffraction peaks, θ is Bragg angle and k = Scherrer's constant (0.89). On the basis of obtained data the average anticipated crystallographic size was found between 15-25 nm.

FESEM analysis:

Fig 3 (a-d) depict the FESEM (field emission scanning electron microscopy) micrographs of (ASB), (LaCF) and (ASB/LaCF) nanocomposites at various magnifications. In **Fig 3 (a)**, the clean, smooth, and porous surface of ASB has been identified. This porous structure clarifies to the volatile chemicals emission while carbonization process **[23]**.

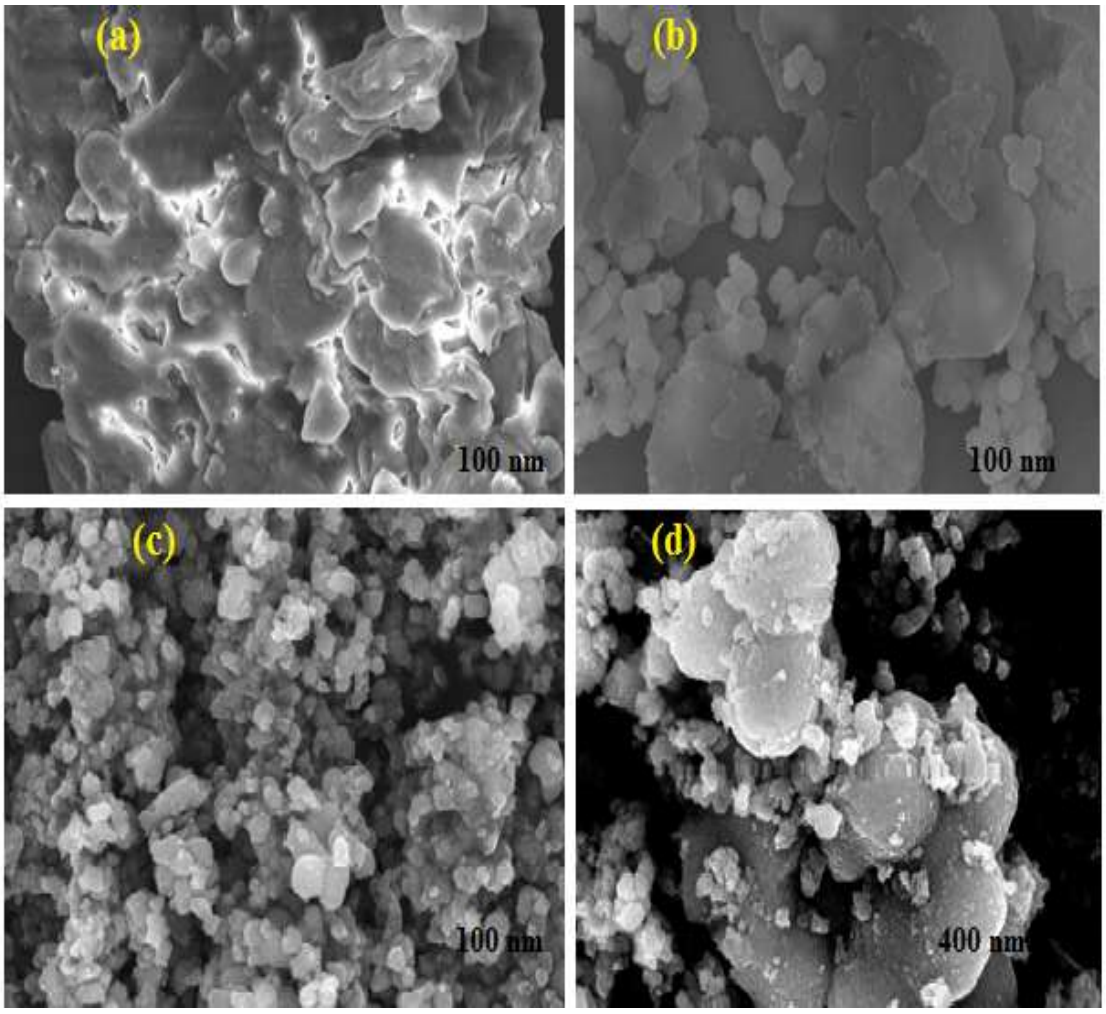

Fig 3: FESEM images spectra of (a) ASB, (b) LaCF and (c) & (d) ASB/LaCF at different magnification

(LaCF) as shown in **Fig 3 (b)**, exhibit tiny spherical and multilayered structures, indicating incorporation of all three salts in homogenous fashion. **Fig 3 (c-d)** described the images of nanocomposite at 100 nm and 400 nm respectively that illustrated the emergence of tiny spherical structures of (LaCF) within the porous matrix of ASB with random distribution on its surface **[24-25]**. Additionally, thousands of nano-holes were clearly observed on the surface of SCB/NC.

VSM Study:

The magnetic property of the ASB/LaCF nanocomposite was determined by vibrating sample magnetometer (VSM) at room temperature in an applied magnetic field sweeping from -2000 to 2000 G **(Fig 4)** and the hysteresis loop passes via Cartesian-axis which indicates that the ASB/LaCF nanocomposite possesses superparamagnetic behavior with no coercivity or retentivity. Because of nil retentivity the material was regarded as soft **[26]**. The saturation magnetization value of synthesized composite was found to be 0.354 emu/g.

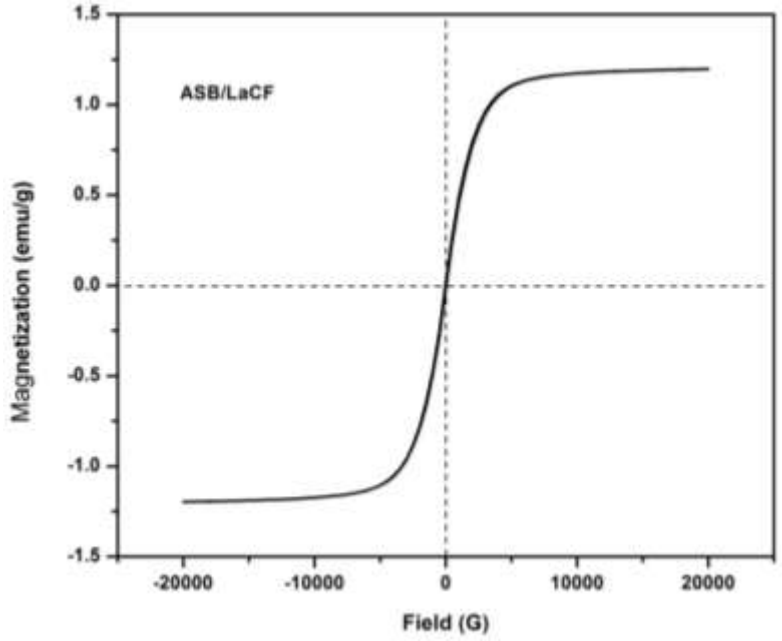

Fig 4: VSM graph of ASB/LaCF Nanocomposite

BET analysis:

The porosity of a material is an essential requirement for the sorption of impurities from a water sample. The pore size has fragmented into the three main groups i.e. macroporous (>50 nm), mesoporous (2-50 nm) and microporous (<2 nm) **[27]**. The BJH (Barrett–Joyner–Halenda) model by utilizing nitrogen desorption branch of isotherm was deployed to examine the pore size distribution of ASB **(Fig 5 (a))** and ASB/LaCF **(Fig 5 (b))**. The highest diameter of ASB was observed 3.2 nm while for ASB/LaCF nano-structure it was 7.5 nm **[28]**.

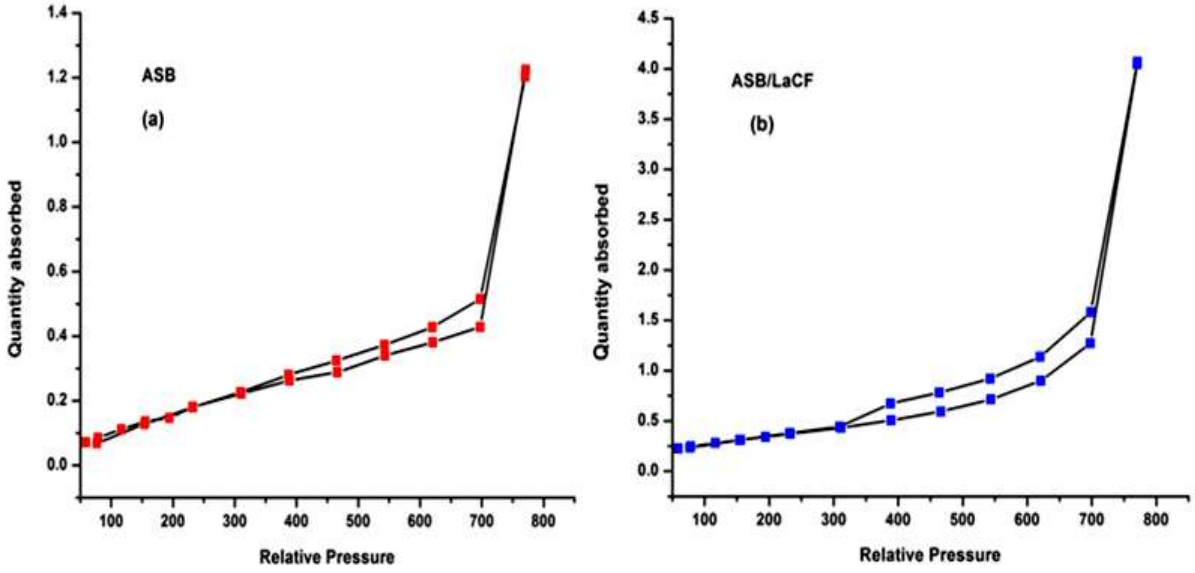

Fig 5: BET isotherm showing adsorption and desorption of (a) ASB and (b) ASB/LaCF Nanocomposite

Hence, the synthesized nano-hybrid structure was found in the range of mesoporous nanocomposite, which might be responsible for the maximum adsorption uptake of Alizarin red S dye from water system. The BET surface area of ASB/LaCF nano-hybrid was observed as 52.25 m^2/g.

TGA and DSC Analysis:

TGA curve shown in the **(Fig 6)** depicted the loss in weight percentage with respect to the temperature. On raising the temperature, there was reduction in weight due to changes observed in composition of the tested compound (ASB/LaCF). This was inferred from **(Fig 6)** that there was almost 3 % decrease in weight up to 97 ^{0}C, which suggest the loss of water in the form of moisture from the sample (ASB/LaCF). When the temperature raised around 200 ^{0}C,

further 50 % weight loss was established. This loss in weight may be due to breakage of bond or decomposition of organic content i.e. leaf extract available in sample. The 10 % weight loss was identified up to temperature of 250 ^{0}C which confirm loss of metal oxygen bond in the nanocomposite (ASB/LaCF) **[29]**.

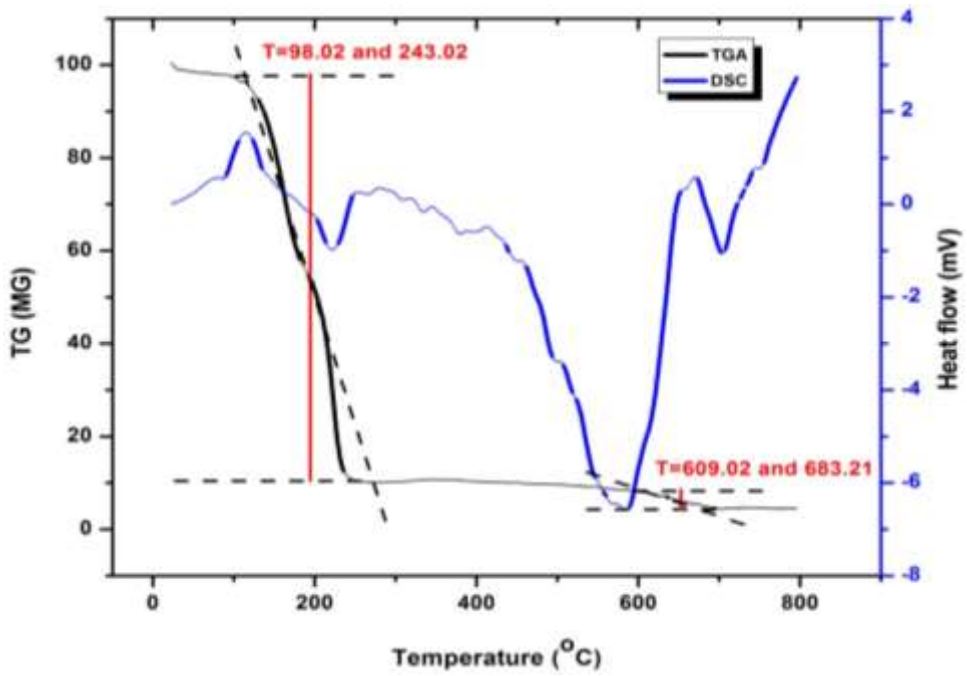

Fig 6: TGA and DSC graph of ASB/LaCF Nanocomposite

This is confirmed that above 400 ^{0}C, the bio-nanocomposite (ASB/LaCF) was comparatively more stable. Steady decrease in weight continued up to 700 ^{0}C expressing that (ASB/LaCF) was more stable at high range of temperature **[30]**. Similar pattern of heat flow has been observed in DSC graph of (ASB/LaCF) **(Fig 6)** where almost identical peaks have been identified the co-ordinate with values of TGA graph **(Fig 6).**

Effect of experimental conditions on Alizarin red S dye adsorption (Parameter optimization):

Effect of contact time:

The contact time and dye removal efficiency are directly related to each other up to an equilibrium point i.e. the removal efficiency keeps on increasing up to the equilibrium **[31]**. The range of the Alizarin red S dye removal by ASB and ASB/LaCF adsorbents was monitored by adjusting the contact time from 10 min to 60 min and the concentrations of dye ranged from 50 to 250 mg/L. The other adsorption applicable like temperature 30 °C, pH 2, and dose rate 0.2 g and 0.1 g (ASB and ASB/LaCH) were kept constant. The impact of the shaking time was graphically shown in **(Fig 7)**. It is evident from the figures that, there was a tremendous rise in the elimination of dye molecules up to 40 min, and after that, there was a gradual constant in the elimination of Alizarin red S dye particles in both ASB and ASB/LaCF adsorbents **(Fig 7 (a) and (b))**. To understand it another way, the Alizarin red S dye molecules will have more active sites to connect to the adsorbent surface before 40 min; however, after half an hour, the active sites might be filled with Alizarin red S dye molecules **[32]**. The percentage of adsorption in case of ASB/LaCF **(Fig 7 (b))** was found increased when compared with adsorption percentage of ASB **(Fig 7 (a))**.

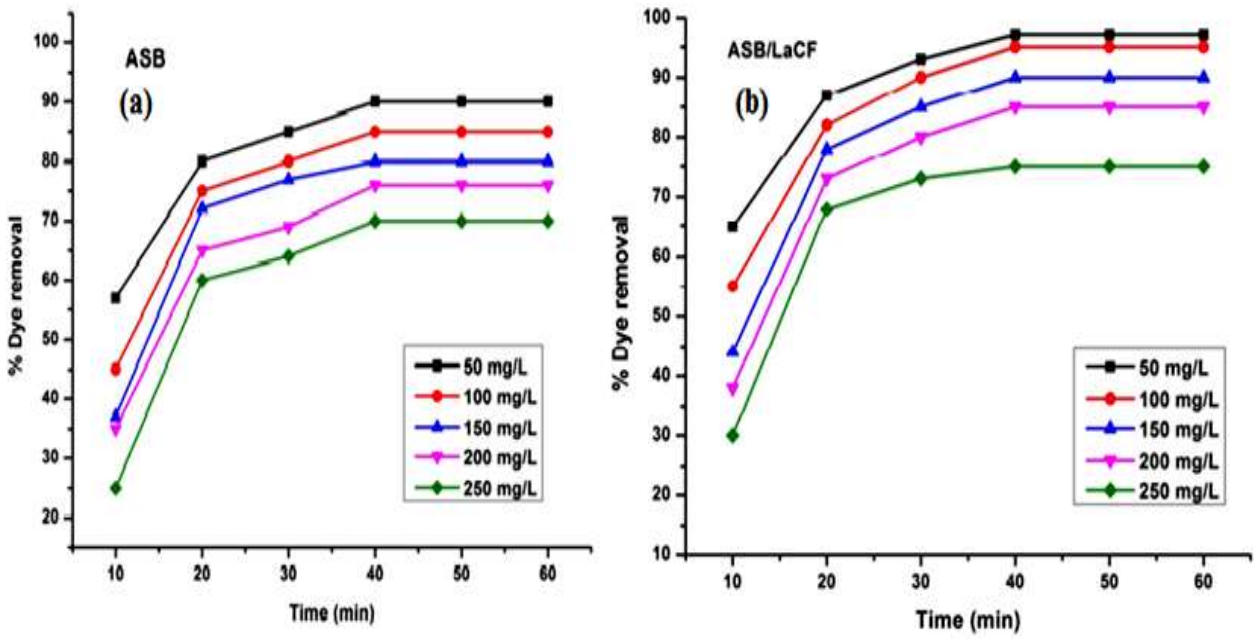

Fig 7: Effect of contact time for the elimination Alizarin red S dye by (a)ASB and (b) ASB/LaCF at different concentrations

Effect of Initial concentration:

To investigate how the initial dye concentration influences adsorption, Alizarin red S dye concentrations were varied from 50 to 250 mg/L, while other conditions i.e. pH 2, contact time, temperature, and adsorbent dosages of 0.2 g (ASB) and 0.1 g (ASB/LaCF) were kept constant. **(Fig 8)** illustrates the removal efficiencies of Alizarin red S dye using ASB and ASB/LaCF adsorbents. As shown, the adsorption efficiency progressively decreases with increasing dye concentration, dropping from 97.25% to 84.41% for (ASB/LaCF) and from 96.51% to 76.71% for (ASB). This decline occurs because, at higher dye concentrations, a larger number of Alizarin red S dye molecules compete for the limited active sites available on the adsorbent surface. Despite the change in initial concentrations, the number of active sites remains constant, allowing only a fixed amount of dye to be removed **[33]**.

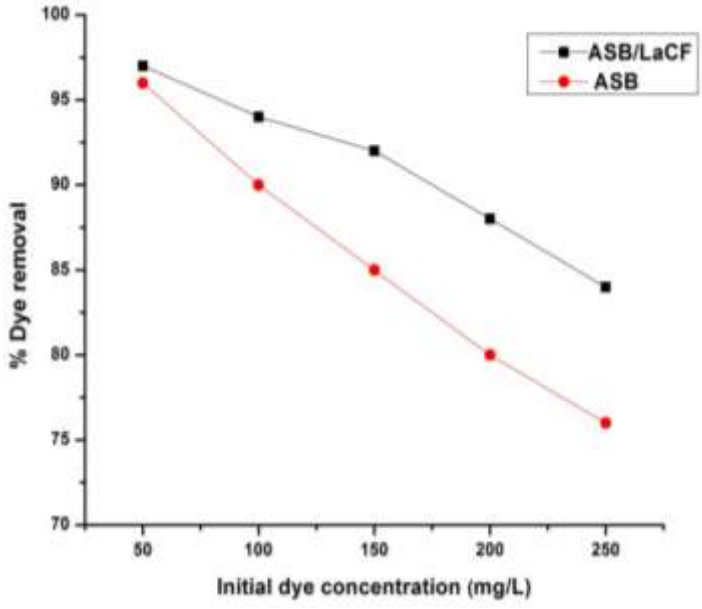

Fig 8: Effect of concentration on the elimination of Alizarin red S dye by ASB and ASB/LaCF

Impact of the pH:

The influence of pH on the adsorption efficiency of Alizarin red S dye using ASB and ASB/LaCH adsorbents was examined by adjusting the solution pH from 2 to 10, while keeping other parameters constant: adsorbent dosage (0.2 g for ASB and 0.1 g for ASB/LaCF), temperature (30 °C), shaking time (60 min), and dye concentration (50 mg/L). **(Fig 9)** shows the percentage removal of Alizarin red S dye at different pH levels, indicating a clear decline in adsorption efficiency as pH increases from 2 to 10. Maximum removal 99.85% for ASB and 99.91% for ASB/LaCF occurred at pH 2, confirming that the adsorption process is favored under acidic conditions. The presence of sulfonic acid groups causes Alizarin red S dye molecules to carry a negative charge in aqueous solutions. The pHZPC {ZPC}ZPC values of ASB and ASB/LaCF, determined using the pH drift method, were 6.25 and 6.34, respectively **[34]**. Thus, at pH 2 (pH < Phzpc {ZPC}ZPC), the adsorbent surfaces are positively charged, promoting strong electrostatic attraction between the dye molecules and the adsorbents hence the high adsorption efficiency.
Across the pH range of 2–10, the efficiency decreased from 99% to 30% for ASB and from 99% to 25% for ASB/LaCF. This decline is attributed to the electrostatic repulsion that occurs when both the dye molecules and the adsorbent surfaces become negatively charged at higher pH levels **[35]**.

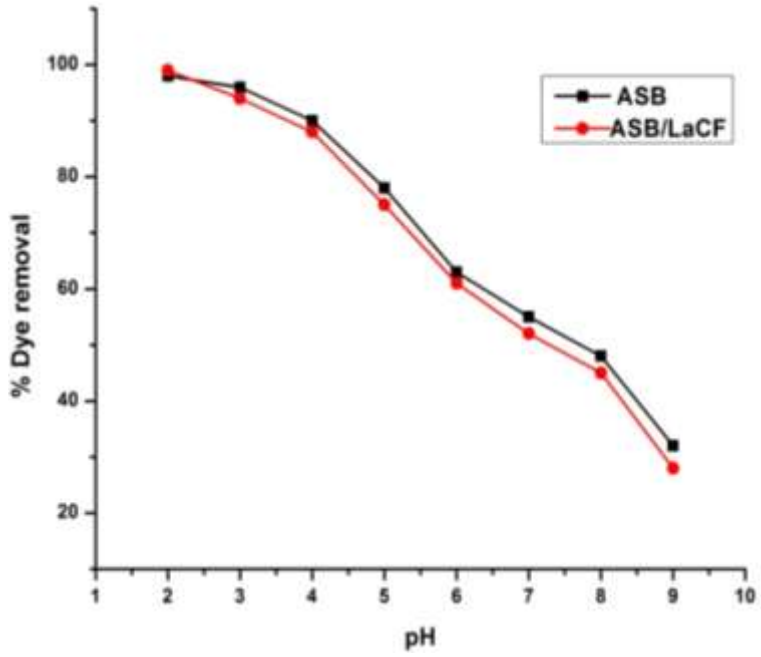

Fig 9: Effect of pH on the elimination of Alizarin red S dye by ASB and ASB/LaCF

Effect of Dosage:

To assess the effect of adsorbent dosage on Alizarin red S dye removal, ASB dosages were varied from 0.5 to 3 g, while ASB/LaCF dosages ranged from 0.25 to 2 g, with all mentioned adsorption parameters kept constant. As shown in **(Fig 10 (a)** and **(b))**, the removal efficiency of Alizarin red S dye increased from 35.55% to 97.85% for ASB **(Fig 10 (a))** and from 65.69% to 98.96% for ASB/LaCF **(Fig 10 (b))** as the adsorbent dosage increased **[36]**. This improvement is attributed to the greater surface area and the higher number of active sites available at higher dosages. Equilibrium was reached at dosages of 2.0 g for ASB and 0.9 g for ASB/LaCF. Beyond these points, further increases in adsorbent mass did not enhance removal efficiency, as the fixed dye concentration provided no additional Alizarin red S dye molecules to occupy newly added active sites **[37]**. The superior performance of ASB/LaCF compared to ASB is primarily due to its larger surface area.

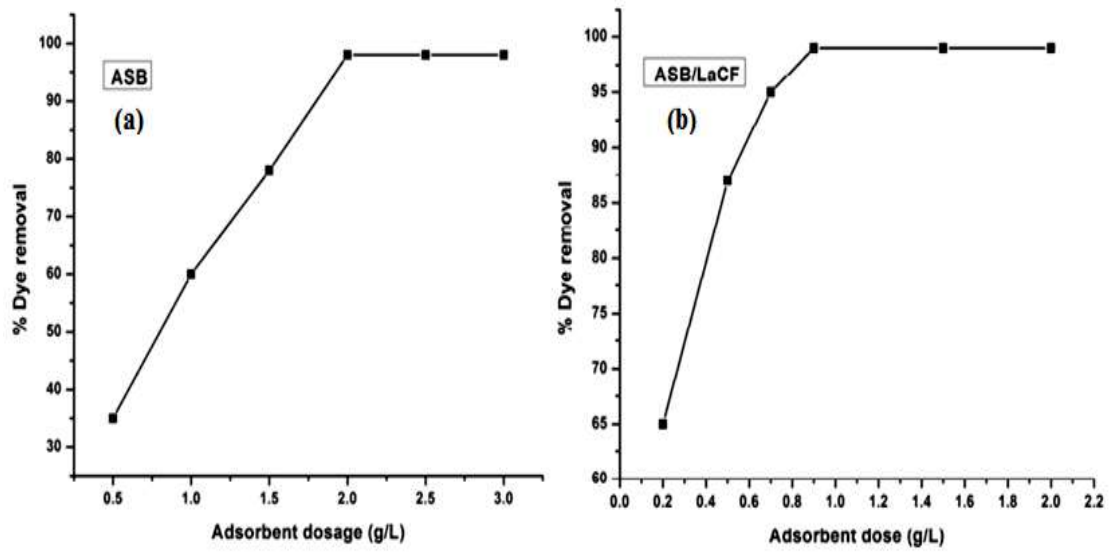

Fig 10: Effect of dosage on the elimination of Alizarin red S dye by (a) ASB and (b) ASB/LaCF

Impact of temperature:

The influence of temperature on Alizarin red S dye removal using ASB and ASB/LaCF adsorbents was investigated by varying the temperature from 303 K to 333 K while keeping all other experimental parameters constant. **(Fig 11 (a)** and **(b))** present the percentage removal of Alizarin red S dye at different temperatures. The results clearly indicate that increasing the temperature adversely affects the adsorption process. At lower temperatures (303 K), the kinetic energy of the system is reduced, which enhances adsorption efficiency. This is primarily due to the stronger attractive interactions between the protonated adsorbent surfaces (ASB and ASB/LaCF) and deprotonated Alizarin red S dye molecules **[38-39]**. As the temperature rises, the kinetic energy of the dye molecules increases, intensifying electrostatic repulsion between the adsorbents and the dye. Consequently, higher temperatures promote the desorption of Alizarin red S dye molecules from the adsorbent surface, resulting in reduced removal efficiency.

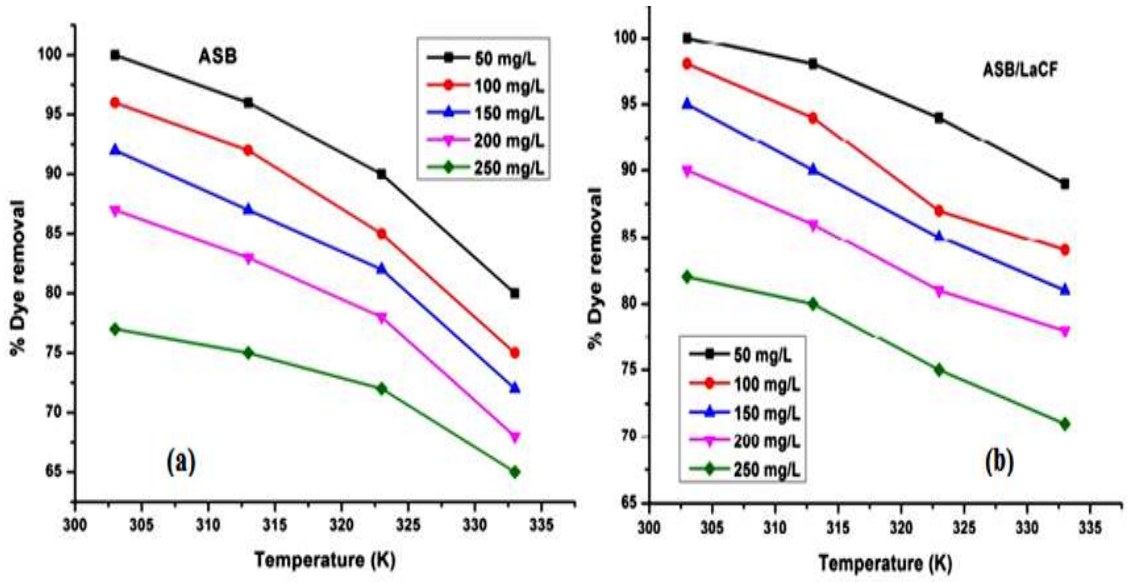

Fig 11: Effect of temperature on the elimination of Alizarin red S dye by (a) ASB and (b) ASB/LaCF

Thermodynamic studies:

In general, adsorption isotherms describe the retention, release, and mobility of adsorbate molecules on a solid surface at a constant temperature after their introduction into an aqueous medium. These isotherms are essential for understanding the mechanisms governing adsorption, and they provide critical insight into the overall efficiency of the

process **[40-41]**. The Langmuir adsorption isotherm is one of the most widely applied models for evaluating surface interactions. It assumes a homogeneous surface and describes adsorption as a monolayer process.
Mathematically, the Langmuir adsorption isotherm model is given by **[42]**:

$$q_e = \frac{q_m K_L C_e}{1 + K_L C_e} \quad \text{..... (4)}$$

Here, Ce, qm, and ilibrium concentration, the maximum adsorption capacity, and the amount of dye adsorbed at equilibrium, expressed in mg L^{-1}, mg g^{-1}, and mg g^{-1}, respectively. K_L (L mg^{-1}) represents the Langmuir isotherm constant.
Another form of the Langmuir adsorption isotherm is the Freundlich isotherm model, which describes a multilayer adsorption process. It is expressed as follows **[43]**:

$$q_e = K_F C_e^{1/n} \quad \text{..... (5)}$$

The Freundlich coefficient *n* indicates the intensity or favorability of the adsorption process, while the constant $K_{(F)}$ is expressed as [(mg g^{-1})(L mg^{-1})$^{1/n}$].
The Temkin isotherm model suggests that interactions between the adsorbent and adsorbate cause the heat of adsorption to decrease linearly with increasing coverage. The mathematical form of the Temkin isotherm model is given below:

$$q_e = B \ln (A_T C_e) \quad \text{..... (6)}$$

$$B = RT/b_T \quad \text{..... (7)}$$

The parameters B, R, T, and A_t correspond to the heat of adsorption (J/mol), the absolute temperature (K), the Temkin isotherm constant (b_T), and the Temkin equilibrium binding constant (L/mg), respectively.

The three-parameter Redlich–Peterson isotherm is an empirical model that incorporates features of both the Freundlich and Langmuir isotherms **[44]**. At higher concentrations, the model behaves similarly to the Freundlich isotherm, while at lower concentrations it aligns w n. Its mathematical form is expressed as follows:

$$q_e = \frac{K_R C_e}{1 + \alpha_R C_e^{\beta}} \quad \text{..... (8)}$$

In this model, K_r (L/g) and α_r (L/ ch–Peterson isotherm constants, while β is a dimensionless exponent associated with adsorption intensity, typically ranging from 0 to 1. The value of β indicates the nature of the adsorption behavior: when β = 1, the system follows the Langmuir isotherm, whereas values less than 1 indicate conformity with the Freundlich model **(Table 1)**. The graphical representations of the isotherm studies are shown in **(Fig 12 (a)** and **(b))**.

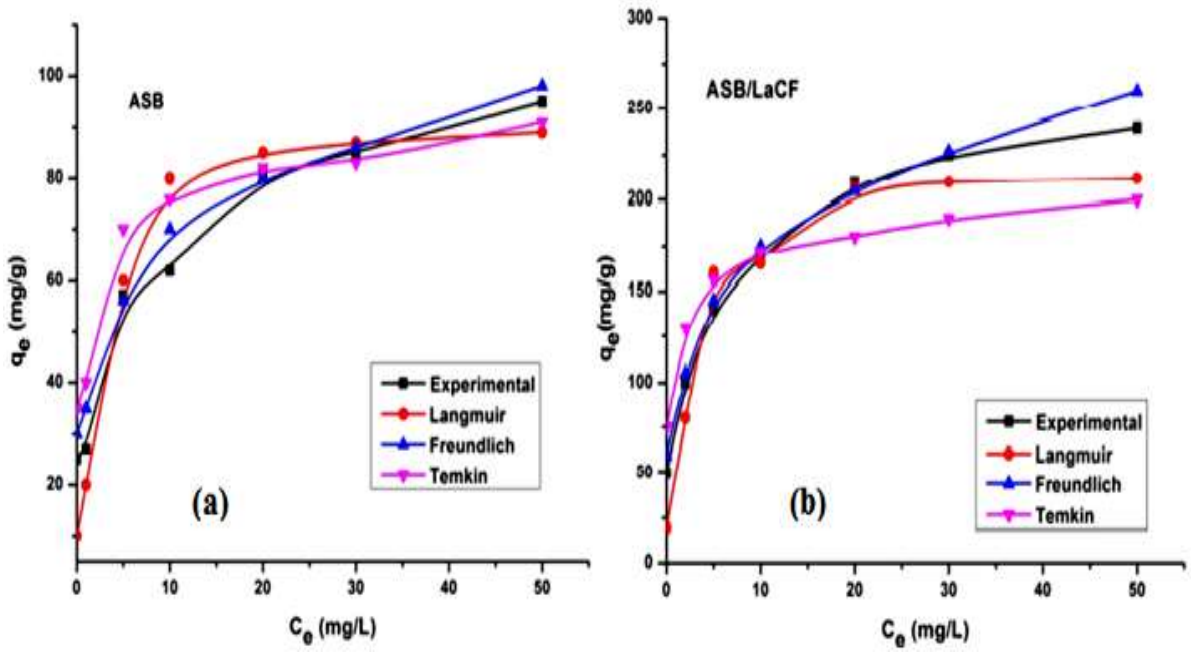

Fig 12: Isotherm assessment of elimination of Alizarin red S dye by (a) ASB and (b) ASB/LaCF

Table 1: Isotherm parameters for Alizarin red S dye removal by ASB and ASB/LaCF

Sr. No.	**Adsorbents**	**ASB**	**ASB/LaCF**
	Parameters	**Alizarin red S dye (Adsorbate)**	**Alizarin red S dye (Adsorbate)**
a)	**Langmuir**		
1.	Q_m (mg/g)	52.79912	99.47271
2.	K_L (L/mg)	0.001	0.03
3.	R_L	0.0196	1.0195
4.	R^2	0.47	0.48
b)	**Freundlich**		
1.	K_F (L/g)	30.73	40.14
2.	n	1.3	3.5
3.	R^2	0.78	0.79
c)	**Tempkin**		
1.	K_T (mg/g/h^2)	10.09	39.85
2.	B (g/mg/ h^2)	9.60	18.36
3.	R^2	0.56	0.56

Adsorption Kinetic Study:

In an adsorption process, kinetic models are crucial because they reveal key information about mass-transfer mechanisms, adsorption efficiency, and the overall rate at which adsorption occurs. These models describe how quickly dye molecules are captured by the adsorbent and how they are later released. In general, adsorption kinetics help determine whether the process follows physical or chemical adsorption. To assess these behaviors, several kinetic models are commonly applied, including the pseudo–first-order, pseudo–second-order, and Elovich models **[45]** whose mathematical expressions are given below.

$$q_t = q_e\,(1-\exp(-k_1 t)) \quad \ldots\ldots\ldots\ldots\ldots\ldots\ldots\ldots\ldots\ldots\ldots\ldots \text{(9)}$$

$$q_t = q_e^2\, k_2 t/1+ q_e k_2 t \quad \ldots\ldots\ldots\ldots\ldots\ldots\ldots\ldots\ldots\ldots\ldots\ldots \text{(10)}$$

$$q_t = 1+\beta_E \mathrm{In}(1+\alpha_E\beta_E t) \ldots\ldots\ldots\ldots\ldots\ldots\ldots\ldots\ldots\ldots\ldots\ldots \text{(11)}$$

Where q_e is the amount of adsorbate adsorbed at equilibrium conditions (mg g^{-1}), q_t is the adsorption capacity at a specific time t (mg/g), k_1 and k_2 are the kinetic rate constants (min^{-1}), α is the initial adsorption rate(mg/g.min) and β is the elovich isotherm constant (g/mg).

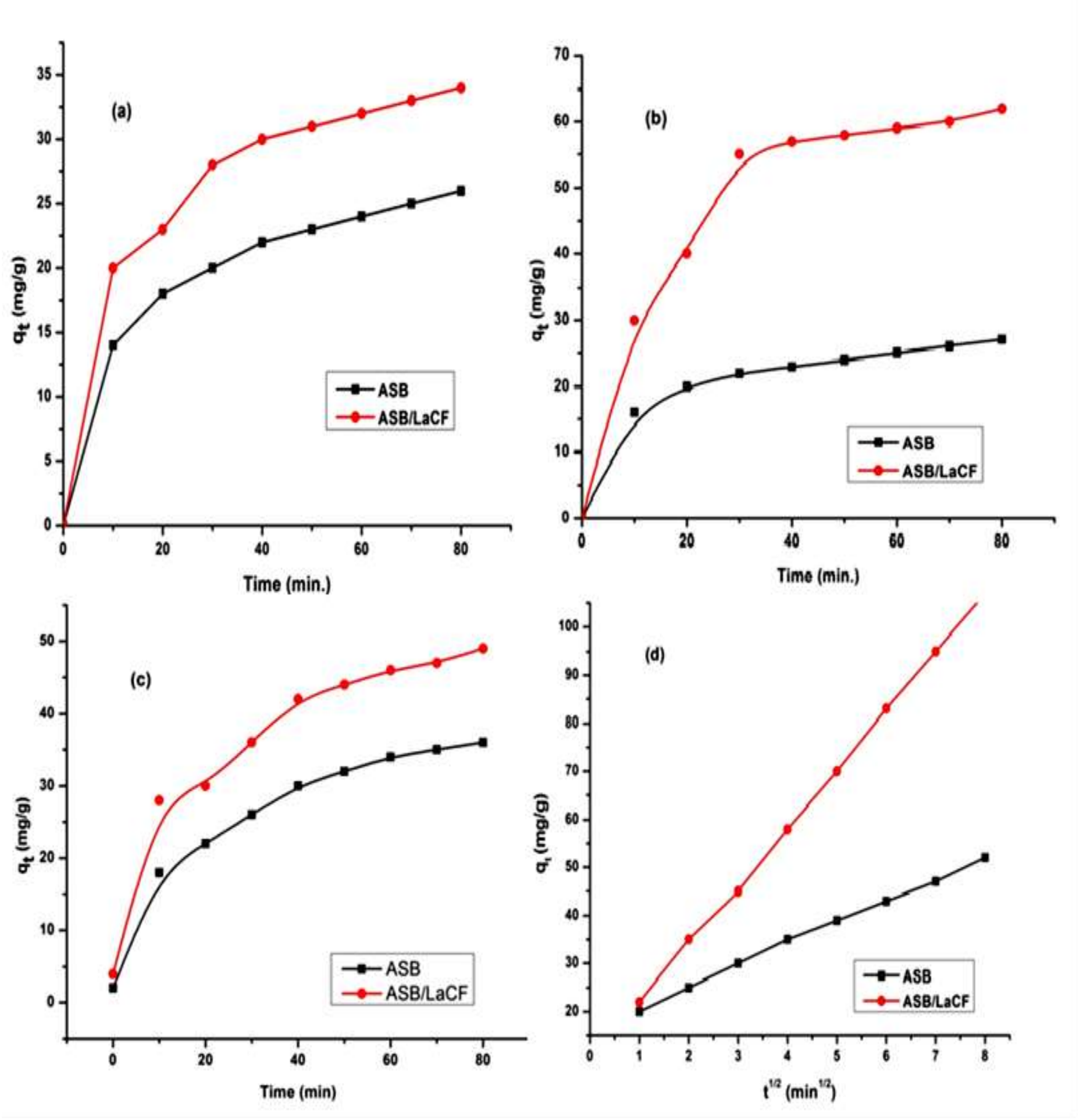

Fig 13: Adsorption Kinetic model assessment (a) pseudo-1st order model, (b) pseudo-2nd order model , (c) Elovich model and (d) diffusion model for ASB and ASB/LaCF

Table 2: Parameters of Adsorption Kinetic model (a) pseudo-1st order model, (b) pseudo-2nd order model , (c) Elovich model and (d) diffusion model for ASB and ASB/LaCF

Sr. No.	Adsorbents	ASB	ASB/LaCF
	Parameters	**Alizarin red S dye (Adsorbate)**	**Alizarin red S dye (Adsorbate)**
a)	**Pseudo-1st order**		
1.	q_e (mg/g)	11.17	18.25
2.	K_1 (1/h)	0.038	0.049
3.	R^2	92.36	95.32
b)	**Pseudo-2nd order**		
1.	q_e (mg/g)	11.25	22.41
2.	K_2 (g/mg/min)	0.03	0.05
3.	R^2	93.25	96.78
c)	**Elovich**		
1.	α(mg/g/h^2)	21.45	46.84
2.	B (g/mg)	0.27	0.34
3.	R^2	96.25	97.14
d)	**Diffusion model**		
1.	C (mg/g)	9.67	16.27
2.	K_{id}(mg g^{-1} $h^{1/2}$	7.85	10.24
3.	R^2	0.99	0.99

The graphical presentation of all kinetic models has been shown in **(Fig 13)** for ASB and ASB/LaCF. The kinetic parameters for all the models have been displayed in **(Table 2)**. The kinetic parameters were examined by analyzing pseudo-1st order model, pseudo-2nd order model and Elovich models. **(Table 2)** validate that the kinetic parameters of Alizarin red S dye adsorption on ASB and ASB/LaCF nanocomposite with high amount of regression coefficient of 0.97 **[46]**. The process of adsorption for Alizarin red S dye from water sample contains within three phases i.e. the first phase found between 20 and 30 minutes, in which ions of Alizarin red S dye migrate from aqueous medium to the surface of adsorbate. The second stage last from 40-60 minutes that can explain the intraparticle diffusion of dye to the internal pores of adsorbate. The last and third stage last upto 80 minutes elaborated the progress of adsorption controlled by pore diffusion **[47]**. Hence, as the plot crosses the origin **(Fig 13 (d))**, it can be concluded that intraparticle diffusion might be the rate limiting parameter.

Thermodynamic Analysis:

The thermodynamic behavior of the system was evaluated using key parameters—Gibbs free energy (ΔG), enthalpy (ΔH), and entropy (ΔS). These parameters are commonly analyzed to determine the feasibility of the adsorption process, identify whether it is exothermic or endothermic, and assess the degree of randomness or disorder involved in the system. For this study, the temperature was varied from 303 K to 333 K while the Alizarin red S dye concentration was kept 50 mg/L. All other conditions, including pH, adsorbent dosage, and contact time, were maintained constant. Gibbs free energy, enthalpy, and entropy were calculated using the equations (12 to 16) presented below.

$$K_C = C_{Ae}/C_e \quad \text{..... (12)}$$

$$\Delta G^o = -RT\ln K_C \quad \text{..... (13)}$$

$$\Delta G^o = \Delta H^o - T\Delta S^o \quad \text{..... (14)}$$

$$\ln K_C = (\Delta H^o/RT) + (\Delta S^o/R) \quad \text{..... (15)}$$

$$\log K_C = (\Delta H^o/2.303RT) + (\Delta S^o/2.303R) \quad \text{..... (16)}$$

The variables C_{Ae}, C_e, T, R, and K_c denote the amount of adsorbate retained on the adsorbent surface (mg/L), the equilibrium concentration of Alizarin red S dye in the aqueous phase (mg/L), the absolute temperature (K), the universal gas constant (8.314 J/mol·K), and the equilibrium constant, respectively.

The thermodynamic parameters obtained for Alizarin red S dye has been summarized in **(Table 3).** At all studied temperatures, the change in Gibbs free energy (**ΔG°**) values were negative and continues increasing on rising the temperature for ASB and ASB/LaCF, confirming that the adsorption process is both thermodynamically feasible and spontaneous **(Fig 14 (a))**. The negative value of enthalpy change (ΔH°) indicates that the adsorption is exothermic in both the cases **[48-49]**. In addition, the negative entropy change (ΔS°) values (J/mol·K) suggest decline in quantity of randomness at the solid–liquid interface during the adsorption of Alizarin red S dye onto the surface of ASB and ASB/LaCF. A comparison between the values of both adsorbate i.e. ASB and ASB/LaCF can be understand easily from **(Table 3)**.

Table 3: Thermodynamic values of adsorption of Alizarin red S dye for ASB and ASB/LaCF

Sr. No.	Temperature	ΔG° (KJ/mol)	
		ASB	ASB/LaCF
1.	300	-4.814	-6.547
2.	313	-4.715	-6.487
3.	323	-4.547	-5.847
4.	333	-4.478	-4.984
5.	ΔH° (KJ/mol)	-5.847	-10.472
6.	ΔS° (J/mol/K)	-26.524	-56.845

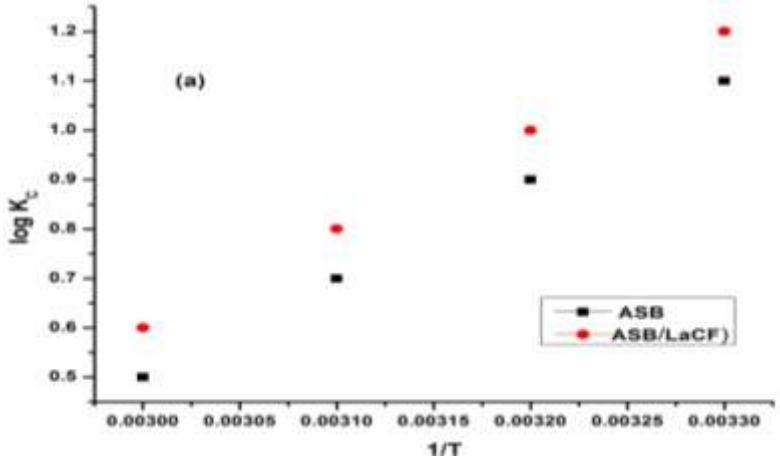

Fig 14: Thermodynamic parameters of adsorption of Alizarin red S dye by ASB and ASB/LaCF

Regeneration analysis:

Typically, spent adsorbents are discarded into the environment as waste, posing significant disposal challenges. These materials can be hazardous and often require energy-intensive and costly methods such as incineration. Direct dumping further contributes to environmental risks. Regenerating spent adsorbents offers an effective solution, providing advantages such as enhanced material stability and the potential recovery of valuable adsorbates.

For this study, NaOH was employed as the eluting agent for regenerating the spent adsorbents. For the regeneration procedure, HC and MHC were first saturated with a 50 mg/L Alizarin red S dye solution for a predetermined contact time. Following saturation, 0.1 M NaOH was used to desorb the dye molecules. The alkalinity of NaOH disrupts the electrostatic and hydrogen-bonding interactions between the Alizarin red S dye and the surface functional groups of ASB and ASB/LaCF, thereby promoting desorption. After desorption, the adsorbents were washed and oven-dried at 150 °C for 120 minutes before reuse.

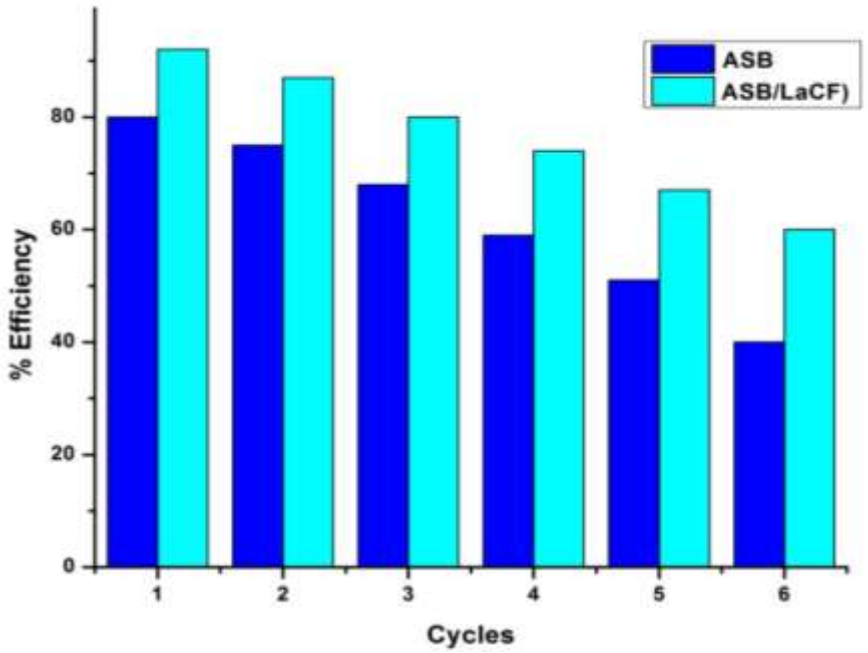

Graph 1: Regeneration of ASB and ASB/LaCF adsorbents.

Both ASB and ASB/LaCF were successfully regenerated for up to sixth cycles, with regeneration efficiencies ranging from 92% to 60% for ASB/LaCF and 80% to 40% for ASB. The regeneration performance is illustrated in **(Graph 1)** showing that ASB/LaCF consistently outperformed ASB across all cycles. After the fifth cycle, ASB/LaCF retained approximately 60% efficiency, whereas ASB declined to about 40%. The gradual reduction in efficiency is likely due to physical and chemical alterations of the adsorbent surface and the loss of functional groups during repeated regeneration **[50-52]**.

Conclusion:

This research article comprises fabrication of two eco-friendly and cost-effective adsorbents named, ASB and ASB/LaCF by utilizing shell of ***Arachis hypogea*** and Lanthanum nitrate ($La(NO_3).6H_2O$), ferric nitrate ($Fe(NO_3).6H_2O$) and cobalt nitrate ($CoNo_3).6H_2O$ as raw materials. The derived biochar and respective nanocomposite were identified through various characterization techniques such as FTIR, XRD, FESEM, TGA, DSC, VSM and BET etc. Results of all these techniques provide information regarding the nature and composition of the synthesized materials. Both ASB (Biochar) and ASB/LaCF (biochar based nanocomposite) were analysed for thermodynamic and kinetic studies by utilizing various models and isotherms through their adsorption efficiency for Alizarin red S dye. The Langmuir, Freundlich and Tempkin isotherm model described the adsorption of Alizarin red S dye efficiently. While kinetic parameters such as Pseudo 1^{st} order, 2^{nd} order and Elovich model along with diffusion model were performed to make sure the high efficiency of synthesized materials. Regeneration test was also performed to analyse the recovery and recyclability of tested biochar (ASB) and respective nanocomposite (ASB/LaCF).

References:

1. Luo L, Wang G, Shi G, Zhang M, Zhang J, He J, Xiao Y, Tian D, Zhang Y, Deng S, Zhou W. The characterization of biochars derived from rice straw and swine manure, and their potential and risk in N and P removal from water. Journal of Environmental Management. 2019 Sep 1;245:1-7.
2. Qian TT, Wu P, Qin QY, Huang YN, Wang YJ, Zhou DM. Screening of wheat straw biochars for the remediation of soils polluted with Zn (II) and Cd (II). Journal of hazardous materials. 2019 Jan 15;362:311-7.
3. Yargicoglu EN, Sadasivam BY, Reddy KR, Spokas K. Physical and chemical characterization of waste wood derived biochars. Waste management. 2015 Feb 1;36:256-68.
4. Babu BV, Chaurasia AS. Modeling, simulation and estimation of optimum parameters in pyrolysis of biomass. Energy Conversion and Management. 2003 Aug 1;44(13):2135-58.
5. Sharma A, Pareek V, Zhang D. Biomass pyrolysis—A review of modelling, process parameters and catalytic studies. Renewable and sustainable energy reviews. 2015 Oct 1;50:1081-96.

6. Kambo HS, Dutta A. A comparative review of biochar and hydrochar in terms of production, physico-chemical properties and applications. Renewable and Sustainable Energy Reviews. 2015 May 1;45:359-78.
7. Varjani S, Kumar G, Rene ER. Developments in biochar application for pesticide remediation: current knowledge and future research directions. Journal of environmental management. 2019 Feb 15;232:505-13.
8. Mohanty SK, Valenca R, Berger AW, Yu IK, Xiong X, Saunders TM, Tsang DC. Plenty of room for carbon on the ground: Potential applications of biochar for stormwater treatment. Science of the total environment. 2018 Jun 1;625:1644-58.
9. Barrow CJ. Biochar: potential for countering land degradation and for improving agriculture. Applied Geography. 2012 May 1;34:21-8.
10. Deonikar VG, Kulkarni VD, Rathod SM, Kim H. Fabrication and characterizations of structurally engineered lanthanum substituted nickel-cobalt ferrites for the analysis of electric and dielectric properties. Inorganic Chemistry Communications. 2020 Sep 1;119:108074.
11. Aslam A, Rehman AU, Amin N, un Nabi MA, ul ain Abdullah Q, Morley NA, Arshad MI, Ali HT, Yusuf M, Latif Z, Mehmood K. Lanthanum doped Zn0. 5Co0. 5LaxFe2− xO4 spinel ferrites synthesized via co-precipitation route to evaluate structural, vibrational, electrical, optical, dielectric, and thermoelectric properties. Journal of Physics and Chemistry of Solids. 2021 Jul 1;154:110080.
12. Nasirpouri F, Fallah S, Ahmadpour G, Moslehifard E, Samardak AY, Samardak VY, Ognev AV, Samardak AS. Microstructure, ion adsorption and magnetic behavior of mesoporous γ-Fe 2 O 3 ferrite nanoparticles. RSC advances. 2023;13(36):25140-58.
13. Chun Y, Zhu Y, Stubenrauch C, Lu Y, Rojas OJ. Biobased ordered porous materials in the nano-to microscales. Current Opinion in Colloid & Interface Science. 2024 Oct 1;73:101822.
14. Mariosi FR, Venturini J, da Cas Viegas A, Bergmann CP. Lanthanum-doped spinel cobalt ferrite (CoFe2O4) nanoparticles for environmental applications. Ceramics International. 2020 Feb 15;46(3):2772-9.
15. Meng X, Li Y, Liu Y, Zhou R, Fu Y, Chen J. Degradation of organic pollutants through activating bisulfite with lanthanum ferrite-loaded biomass carbon. RSC advances. 2023;13(35):24819-29.
16. Jung KW, Lee S, Lee YJ. Synthesis of novel magnesium ferrite (MgFe2O4)/biochar magnetic composites and its adsorption behavior for phosphate in aqueous solutions. Bioresource technology. 2017 Dec 1;245:751-9.
17. Duman G. Preparation of novel porous carbon from hydrothermal pretreated textile wastes: Effects of textile type and activation agent on structural and adsorptive properties. Journal of Water Process Engineering. 2021 Oct 1;43:102286.
18. Abdel-Khalek EK, Ibrahim I, Salama TM. Dielectric anomaly in the microwave region and exchange bias effect in LaFeO3 nanoparticles at room temperature. Ferroelectrics. 2019 Oct 3;550(1):210-9.
19. Senthil VP, Gajendiran J, Raj SG, Shanmugavel T, Kumar GR, Reddy CP. Study of structural and magnetic properties of cobalt ferrite (CoFe2O4) nanostructures. Chemical Physics Letters. 2018 Mar 1;695:19-23.
20. Anjum S, Tufail R, Rashid K, Zia R, Riaz S. Effect of cobalt doping on crystallinity, stability, magnetic and optical properties of magnetic iron oxide nano-particles. Journal of Magnetism and Magnetic Materials. 2017 Jun 15;432:198-207.
21. Covaliu CI, Jitaru I, Paraschiv G, Vasile E, Biriş SŞ, Diamandescu L, Ionita V, Iovu H. Core–shell hybrid nanomaterials based on CoFe2O4 particles coated with PVP or PEG biopolymers for applications in biomedicine. Powder technology. 2013 Mar 1;237:415-26.
22. Nlebedim IC, Snyder JE, Moses AJ, Jiles DC. Effect of deviation from stoichiometric composition on structural and magnetic properties of cobalt ferrite, CoxFe3− xO4 (x= 0.2 to 1.0). Journal of Applied Physics. 2012 Apr 1;111(7).
23. Zhu G, Xing X, Wang J, Zhang X. Effect of acid and hydrothermal treatments on the dye adsorption properties of biomass-derived activated carbon. Journal of Materials Science. 2017 Jul;52(13):7664-76.
24. Said A, Tekasakul S, Phoungthong K. Investigation of hydrochar derived from male oil palm flower: characteristics and application for dye removal. Pol J Environ Stud. 2020 Jan 1;29(1):807-16.
25. Tran TH, Le AH, Pham TH, Nguyen DT, Chang SW, Chung WJ, Nguyen DD. Adsorption isotherms and kinetic modeling of methylene blue dye onto a carbonaceous hydrochar adsorbent derived from coffee husk waste. Science of the Total Environment. 2020 Jul 10;725:138325.

26. Elnour AY, Alghyamah AA, Shaikh HM, Poulose AM, Al-Zahrani SM, Anis A, Al-Wabel MI. Effect of pyrolysis temperature on biochar microstructural evolution, physicochemical characteristics, and its influence on biochar/polypropylene composites. Applied sciences. 2019 Mar 18;9(6):1149.
27. Sewu DD, Jung H, Kim SS, Lee DS, Woo SH. Decolorization of cationic and anionic dye-laden wastewater by steam-activated biochar produced at an industrial-scale from spent mushroom substrate. Bioresource technology. 2019 Apr 1;277:77-86.
28. Venkatesan S, Baloch HA, Jamro IA, Rafique N. Evaluation of the production of hydrochar from spent coffee grounds under different operating conditions. Journal of Water Process Engineering. 2022 Oct 1;49:103037.
29. Oumabady S, S PS, Kamaludeen SP, Ramasamy M, Kalaiselvi P, Parameswari E. Preparation and characterization of optimized hydrochar from paper board mill sludge. Scientific reports. 2020 Jan 21;10(1):773.
30. Gonnella G, Ischia G, Fambri L, Fiori L. Thermal analysis and kinetic modeling of pyrolysis and oxidation of hydrochars. Energies. 2022 Jan 27;15(3):950.
31. Tharayil JM, Chinnaiyan P. Sustainable waste valorisation: Novel Areca catechu L. husk biochar for anthraquinone dye adsorption-Characterization, modelling, kinetics, and isotherm studies. Results in Engineering. 2023 Dec 1;20:101624.
32. Aravindhan S, Kumar GB, Saravanan M, Arumugam A. Delonix regia biomass as an eco-friendly biosorbent for effective Alizarin Red S textile dye removal: Characterization, kinetics, and isotherm studies. Bioresource Technology Reports. 2024 Feb 1;25:101721.
33. Lata H, Mor S, Garg VK, Gupta RK. Removal of a dye from simulated wastewater by adsorption using treated parthenium biomass. Journal of Hazardous Materials. 2008 May 1;153(1-2):213-20.
34. Gautam RK, Banerjee S, Gautam PK, Rawat V, Kumar A, Singh SK, Chattopadhyaya MC. Biosorption of an Acidic Dye, Alizarin Red S, Onto biosorbent of mustard husk: Kinetic, equilibrium modeling and spectroscopic analysis. Asian Journal of Research in Chemistry. 2014;7(4):417-25.
35. Dawood S, Sen TK. Removal of anionic dye Congo red from aqueous solution by raw pine and acid-treated pine cone powder as adsorbent: equilibrium, thermodynamic, kinetics, mechanism and process design. Water research. 2012 Apr 15;46(6):1933-46.
36. Dogar S, Nayab S, Farooq MQ, Said A, Kamran R, Duran H, Yameen B. Utilization of biomass fly ash for improving quality of organic dye-contaminated water. ACS omega. 2020 Jun 22;5(26):15850-64.
37. Akhil D, Lakshmi D, Kartik A, Vo DV, Arun J, Gopinath KP. Production, characterization, activation and environmental applications of engineered biochar: a review. Environmental Chemistry Letters. 2021 Jun;19(3):2261-97.
38. Nazir R, Khan M, Rehman RU, Shujah S, Khan M, Ullah M, Zada A, Mahmood N, Ahmad I. Adsorption of selected azo dyes from an aqueous solution by activated carbon derived from Monotheca buxifolia waste seeds. Soil Water Res. 2020 Sep 30;15(3):166-72.
39. Danso-Boateng E, Fitzsimmons M, Ross AB, Mariner T. Response surface modelling of methylene blue adsorption onto seaweed, coconut shell and oak wood hydrochars. Water. 2023 Mar 3;15(5):977.
40. Yagub MT, Sen TK, Afroze S, Ang HM. Dye and its removal from aqueous solution by adsorption: a review. Advances in colloid and interface science. 2014 Jul 1;209:172-84.
41. Munagapati VS, Wen HY, Vijaya Y, Wen JC, Wen JH, Tian Z, Reddy GM, Raul Garcia J. Removal of anionic (Acid Yellow 17 and Amaranth) dyes using aminated avocado (Persea americana) seed powder: adsorption/desorption, kinetics, isotherms, thermodynamics, and recycling studies. International Journal of Phytoremediation. 2021 Jul 29;23(9):911-23.
42. Langmuir I. The adsorption of gases on plane surfaces of glass, mica and platinum. Journal of the American Chemical society. 1918 Sep;40(9):1361-403.
43. Freundlich HM. Over the adsorption in solution. J. Phys. chem. 1906 Mar;57(385471):1100-7.
44. Malarvizhi R, Ho YS. The influence of pH and the structure of the dye molecules on adsorption isotherm modeling using activated carbon. Desalination. 2010 Dec 15;264(1-2):97-101.
45. Hu Q, Pang S, Wang D. In-depth insights into mathematical characteristics, selection criteria and common mistakes of adsorption kinetic models: A critical review. Separation & Purification Reviews. 2022 Jul 3;51(3):281-99.
46. Kim DG, Choi D, Cheon S, Ko SO, Kang S, Oh S. Addition of biochar into activated sludge improves removal of antibiotic ciprofloxacin. J Water Process Eng 33: 101019 [Internet]. 2020.

47. Abdel-Gawwad HA, Mohammed MS, Arif MA, Shoukry H. Reuse of lead glass sludge in the fabrication of thermally insulating foamed glass with outstanding properties and high Pb-stabilization. Environmental Science and Pollution Research. 2022 Jul;29(31):47209-24.
48. Zhang Z, Xu L, Liu Y, Feng R, Zou T, Zhang Y, Kang Y, Zhou P. Efficient removal of methylene blue using the mesoporous activated carbon obtained from mangosteen peel wastes: Kinetic, equilibrium, and thermodynamic studies. Microporous and Mesoporous Materials. 2021 Feb 1;315:110904.
49. Nodehi R, Shayesteh H, Rahbar-Kelishami A. Fe3O4@ NiO core–shell magnetic nanoparticle for highly efficient removal of Alizarin red S anionic dye. International Journal of Environmental Science and Technology. 2022 Apr;19(4):2899-912.
50. Chieng HI, Lim LB, Priyantha N. Enhancing adsorption capacity of toxic malachite green dye through chemically modified breadnut peel: equilibrium, thermodynamics, kinetics and regeneration studies. Environmental technology. 2015 Jan 2;36(1):86-97.
51. Bhomick PC, Supong A, Baruah M, Pongener C, Sinha D. Pine Cone biomass as an efficient precursor for the synthesis of activated biocarbon for adsorption of anionic dye from aqueous solution: Isotherm, kinetic, thermodynamic and regeneration studies. Sustainable Chemistry and Pharmacy. 2018 Dec 1;10:41-9.
52. Bharath Balji G, Senthil Kumar P. Adsorptive removal of alizarin red S onto sulfuric acid-modified avocado seeds: kinetics, equilibrium, and thermodynamic studies. Adsorption Science & Technology. 2022 Nov 10;2022:3137870.